Transient Electrohydrodynamics of a Liquid Jet: Evolution of The Flow Field

A. Behjatian[1] and A. Esmaeeli[1]

Abstract: Computational studies are performed to explore the underlying physics behind the evolution of the flow field in an around a liquid jet that is immersed in another liquid and is exposed to a uniform electric field. Here the focus is on finite Reynolds and $O(1)$ Ohnesorge number flows. This is achieved by solving the full Navier-Stokes and electric field equations using a front tracking/finite difference technique in the framework of Taylor's leaky dielectric theory. It is shown that the evolution of the flow field is determined by the relative magnitude of the ratio of the electric conductivity $R = \sigma_i/\sigma_o$ and permittivity $S = \varepsilon_i/\varepsilon_o$, where the subscripts i and o denote the fluid inside and outside of the jet. For fluid systems for which $R > S$ or $S > (1/3)(R^2 + R + 1)$ the flow is established by formation of four vortices inside the jet that gradually grow outward until their growth is limited by the jet interface. On the other hands, for fluid systems for which $R < S < (1/3)(R^2 + R + 1)$ the flow evolves through evolution of four vortices that are formed in the ambient fluid and gradually penetrate into the jet until they are confined within the jet. Examination of the electrohydrodynamics of the jets in creeping flows leads to similar observations, and using the closed form analytical solution for these flows the computational and analytical results are justified.

1 Introduction

This study is a follow up to our recent computational investigations [Halim and Esmaeeli (2013)] concerning the transient electrohydrodynamics of a two-dimensional liquid drop (jet) in a uniform DC electric field. There we explored the behavior of the jets with different dielectric properties at $Re = \rho_o u_s a/\mu_o = 1$ and $Oh = \mu_o/\sqrt{\rho_a a \gamma} = 0.5$, u_s, a, and γ being an electrohydrodynamic-driven velocity scale (see Section 2 for definition), the radius of the cross section of the jet, and the surface tension, respectively. For all the cases considered the interface deformed monotonically and acquired a prolate or an oblate shape (resembling an ellipse), depending on the ratios of the dielectric properties of the jet fluid to those of the

---

[1] Southern Illinois University Carbondale.
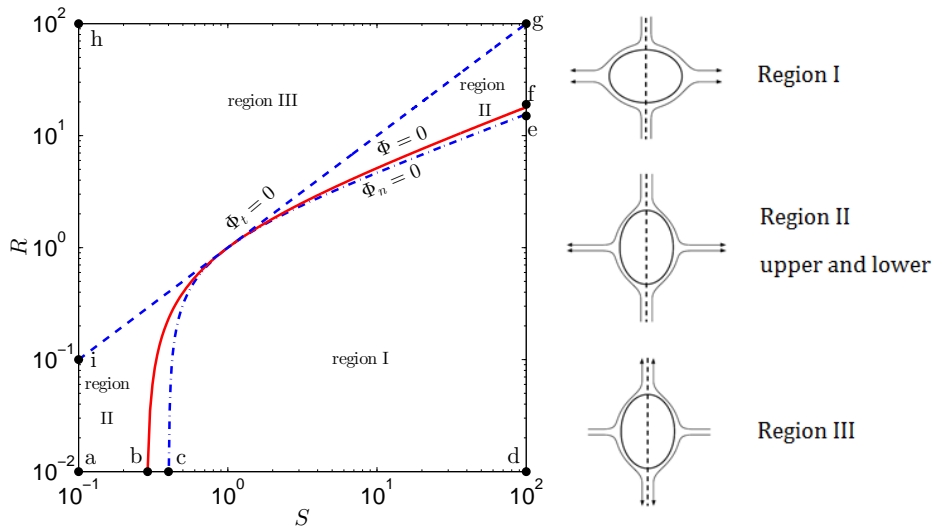
Figure 1: The circulation-deformation map along with the schematics of the steady state flow pattern (top-and-bottom-to-sides vs. sides-to-top-and-bottom) and modes of interface deformation (oblate vs. prolate) in each region. Note that the internal circulation is not shown in the schematics.

ambient fluid. While the structures of the velocity field at an early time and at steady state were also examined, however, the details of the evolution of the flow structure toward steady state were not discussed. Unfortunately, the transient electrohydrodynamics of liquid jets will not be reasonably well understood without gaining a fundamental understanding on the underlying physics of the evolution of the flow pattern. This is because of the two-way coupling between the interface dynamics and the fluid flow, where the interface deformation affects the strength and structure of the flow, and the hydrodynamic stresses in turn affect the interface dynamics. This understanding also finds relevance in a host of microfluidic applications such as enhancement of heat and mass transfer rates [Subramanian and Jog (2005)] and chaotic mixing by electric field [Ward and Homsy (2006)].

To complete the analysis of the problem, therefore, the goal of this study is to provide a detailed understanding of the evolution of the flow field for the cases that were simulated by Halim and Esmaeeli (2013). Interestingly, it turns out that the evolution of the flow pattern for those cases (i.e., $Re = 1$ and $Oh = 0.5$), where inertia $\mathbf{u} \cdot \nabla \mathbf{u}$ and local fluid acceleration $\partial \mathbf{u}/\partial t$ cannot be ignored, is similar to that for a jet in an unbounded domain under the creeping flow regime ($Re \ll 1$) and large Ohnesorge number squared ($Oh^2 \gg 1$) flows, where both fluid inertia

and local fluid acceleration are negligible. As the latter problem has a closed form analytical solution [Esmaeeli and Sharifi (2011)], in this study we will use this solution to interpret and justify the computational observations that will follow.

To put the work in perspective, in the next two paragraphs we provide a brief summary of the steady state [Reddy and Esmaeeli (2009)] and transient [Esmaeeli and Sharifi (2011)] electrohydrodynamics of leaky dielectric liquid jets in a weak electric field.

The key parameters that control the senses of fluid flow and interface deformation at steady state are the ratios of the electric conductivity and permittivity of the jet fluid to the corresponding properties of the ambient fluid; i.e., $R = \sigma_i/\sigma_o$ and $S = \varepsilon_i/\varepsilon_o$, respectively. Here the subscripts i and o denote the fluid inside and outside of the jet. The sense of the fluid circulation in and around the interface at steady state is determined by the relative importance of R and S. For $R > S$ the external flow at the interface runs from the sides to the top and the bottom, for $R < S$ the direction of the flow is reversed, and for $R = S$ the flow ceases to exist [Reddy and Esmaeeli (2009)]. Note that these observations are in line with those for the corresponding problem of an axisymmetric liquid drop in a weak electric field [Taylor (1966)]. The sense of interface deformation at steady state is determined by a characteristic function

$$\Phi = R^2 + R + 1 - 3S. \tag{1}$$

For $\Phi > 0$ the interface becomes prolate (i.e., an ellipse with its major axis parallel to the direction of the electric field), for $\Phi < 0$ the interface becomes oblate (i.e., an ellipse with its major axis perpendicular to the direction of the electric field), and for $\Phi = 0$ the interface remains circular. The steady-state electrohydrodynamics can be best described by considering the so-called circulation-deformation map [Fig. (1)]. This map is constructed by plotting the zero-circulation line [$\Phi_t \equiv R - S = 0$; dashed line] and the zero-deformation curve [$\Phi = 0$; solid line] in $S - R$ coordinates. This results in the three regions shown in Fig. (1) as described below:

$$\text{Region I:} \quad S > \frac{1}{3}(R^2 + R + 1);$$

$$\text{Region II:} \quad R < S < \frac{1}{3}(R^2 + R + 1); \tag{2}$$

$$\text{Region III:} \quad R > S.$$

In region (I), confined between the $\Phi = 0$ curve and the lines $\overline{bd}$ and $\overline{df}$, the interface becomes oblate and the external flow at its surface runs from the top and the bottom toward the sides; in region (II), confined between the $\Phi = 0$ curve and the lines $\Phi_t = 0$, $\overline{ia}$, $\overline{ab}$, and $\overline{fg}$, the interface becomes prolate but the external flow at

its surface still runs from the top and the bottom toward the sides; and in region (III), confined between the $\Phi_t = 0$ line and the lines $\overline{gh}$ and $\overline{hi}$, the interface becomes prolate and the external flow at its surface runs from the sides toward the top and the bottom. Note that Fig. (1) does not show the internal circulation.

The transient electrohydrodynamics of a jet in a weak electric field was studied by Esmaeeli and Sharifi (2011) using a closed form analytical solution. Starting with the momentum equation in nondimensional form

$$\frac{1}{Oh^2}\frac{\partial \mathbf{u}'}{\partial t'} + Re\mathbf{u}' \cdot \nabla'\mathbf{u}' = -\nabla'p' + \nabla'^2\mathbf{u}', \tag{3}$$

the authors considered a weak electric field and a fluid systems for which $Oh^2 \gg 1$ and $Re \ll 1$. Thus, they were able to simplify the momentum equation to quasi-steady state form, $-\nabla'p' + \nabla'^2\mathbf{u}' = 0$, and study the problem by analytical solution. Subsequently they showed that the dynamic is governed by only one characteristic time

$$\tau = \frac{(\mu_i + \mu_o)a}{\gamma}, \tag{4}$$

which is the time scale of the interface deformation, and that the interface deforms monotonically and settles to its steady state deformation according to

$$\mathscr{D} = \mathscr{D}_\infty \left[1 - \exp(-t/\tau) \right], \tag{5}$$

where the deformation parameter $\mathscr{D}$ is defined as

$$\mathscr{D} = \frac{y_{max} - x_{max}}{y_{max} + x_{max}}. \tag{6}$$

Here, y_{max} and x_{max} are the end-to-end length of the jet cross section in the direction of the electric field and the maximum breadth in the traverse direction, respectively, and the steady state deformation is

$$\mathscr{D}_\infty = \frac{Ca}{3}\frac{\Phi}{(R+1)^2}. \tag{7}$$

2   Problem Setup and Nondimensional Parameters

The problem setup is shown in Fig. (2), depicting the cross section of an initially circular liquid jet in a pool of another liquid. The electric field is established by assigning electric potentials ϕ_t and ϕ_b to the top and the bottom walls, respectively.
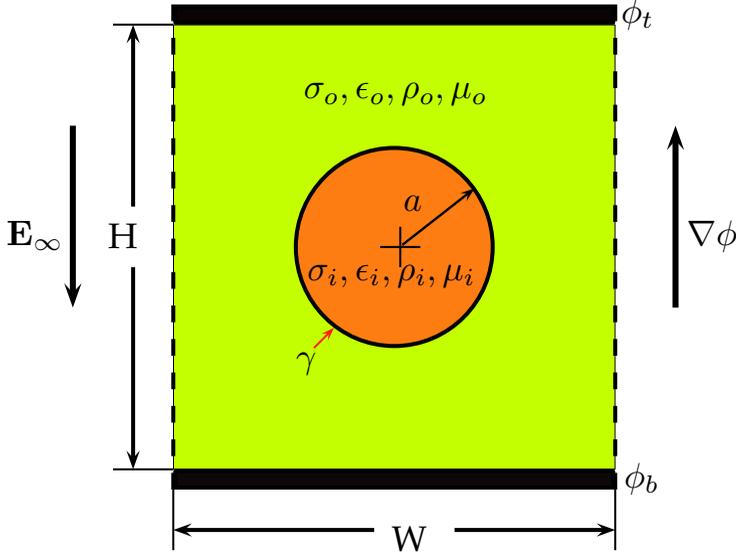
Figure 2: The computational setup, depicting the cross section of a liquid jet of radius a immersed in another liquid. Here ρ, μ, σ, and ε represents, respectively, the density, the viscosity, the electric conductivity, and the electric permittivity. The computational domain is wall-bounded in the vertical direction and periodic in the horizontal direction.

The computational domain is periodic in the horizontal direction and wall-bounded in the vertical direction. No-slip and no-through flow boundary conditions are used for the velocity field at the walls and periodic boundary conditions are used in the horizontal direction.

The physical properties of the fluids are the densities, ρ_i, ρ_o, the viscosities, μ_i, μ_o, the electric permittivities, ε_i, ε_o, and the electric conductivities, σ_i, σ_o. The surface tension is γ. The subscripts i and o denote the physical parameters inside and outside of the jet, respectively. The gravity is set to zero. The governing nondimensional numbers of this problem are $Re_f = \rho_o u_s a/\mu_o$, $Ca = \mu_o u_s/\gamma$, $\alpha = \pi a^2/WH$, $R = \sigma_i/\sigma_o$, $S = \varepsilon_i/\varepsilon_o$, $\widetilde{\rho} = \rho_i/\rho_o$, and $\widetilde{\mu} = \mu_i/\mu_o$. Here, Re_f, Ca, and α are, respectively, the flow Reynolds number, the capillary number, and the volume fraction. Here $u_s = \varepsilon_o E_0^2 a/\mu_o$ is a velocity scale that is constructed by balance of the electric and viscous shear stresses at the interface and $E_0 = |\phi_t - \phi_b|/H$ is a characteristic scale for the electric field strength. It is also customary to consider the Ohnesorge number $Oh = \mu_o/\sqrt{\rho_o a \gamma}$ or the nondimensional strength of the electric field $E^* = \sqrt{Ca} = E_0/\sqrt{\gamma/\varepsilon_o a}$ in lieu of Re_f and Ca, respectively. For leaky dielectric

model to be valid, the time scale of charge relaxation from the bulk to the interface $\tau_C = \varepsilon_o/\sigma_o$ should be much shorter than any process time of interest. As such, $Re_{el} = \tau_C/\tau_P$, which is called the electric Reynolds number, should be sufficiently small. In this study, we consider the convective time scale as the process time of interest, $\tau_P = a/u_s$. Thus, the electric Reynolds number is $Re_{el} = \varepsilon_o u_s/\sigma_o a$.

3   Mathematical Formulation and Numerical Method

The mathematical formulation and the numerical method are based on the "one-fluid" formulation and the front tracking/finite difference technique, respectively, and the governing equations are solved in conjunction with the Taylor's (1966) leaky dielectric theory. We solve the full Navier-Stokes equations for both the fluids in the jet and the ambient. Detailed information regarding the method can be found in Halim and Esmaeeli (2013).

4   Results

4.1   *Computer Simulations*

For all the computations, we considered a jet of radius 0.2 in a computational domain of unit size and resolved the flow using a 256^2 grid. This resulted in about 100 grid points per jet diameter, which is sufficient to accurately resolve the flow based on the grid refinement studies. Here the goal was to explore the effect of the electric properties of the fluids on the evolution of the flow field for the cases that were considered by Halim and Esmaeeli (2013) and also to study the effect of fluid inertia (as represented by Re_f) on the flow field and the jet dynamics. To this end, we performed two sets of simulations for three representative fluid systems (corresponding to the three regions of the map) at $Re_f = 1$ and 10. For all the cases considered, $Oh = 0.45$, $Ca = 0.2$, $\widetilde{\mu} = 1$, $\widetilde{\rho} = 1$, $\alpha = 0.1256$ and $Re_{el} = 5 \times 10^{-3}$. We first report the results for the $Re_f = 1$ case.

We begin our analysis by following the evolution of the flow field for a fluid system from the region (I) of the map by considering $R = \sigma_i/\sigma_o = 2$ and $S = \varepsilon_i/\varepsilon_o = 8$. Figure (3) shows a few frames from this simulation at the selected nondimensional times noted in the caption. The time is nondimensionalized by the characteristic time $\tau = (\mu_i + \mu_o)a/\gamma$. To show the fine structure of the flow, the streamlines are drawn at the selected levels. Therefore, the strength of the flow fields, locally and comparatively, cannot be discerned from this figure. The flow is initiated at the interface as a result of the imbalance of the electric shear stresses and propagates to the rest of the domain through a diffusion process. Shortly after the start of motion ($t/\tau = 0.05$; frame *a*) the flow field consists of four vortices inside the jet that are matched by their counterpart vortices in the ambient fluid. As time progresses the

inner vortices disappear and the outer vortices penetrate inside ($t/\tau = 0.125$; frame *b*). The disappearance of the inner vortices is due to the fact that the deformation-driven flow, which is behind the streamlines that cross the interface, becomes more dominant than the (electric) shear-driven flow, which is behind the formation of the inner vortices. From this point onward, the streamlines that cross the interface start to retreat from the jet as the interface gradually deforms, leading to the reappearance of the inner vortices ($t/\tau = 0.263$ and 2.31; frames *c* and *d*). The fact that in frame (*e*), $t/\tau = 2.8$, a few streamlines still cross the interface is an indication that the interface deformation has not reached a steady state. The flow field eventually settles to steady state as the crossing streamlines retreat further. The flow field at steady state consists of four vortices in the jet that are matched by their counterparts in the ambient fluid ($t/\tau = 7.5$; frame *f*). Here the fluid flow is solely driven by the electric shear stress since the interface no longer deforms. As such, the velocity at the interface is purely tangential. For nearly circular jets in weak electric fields, Reddy and Esmaeeli (2009) showed that the tangential velocity at the interface is
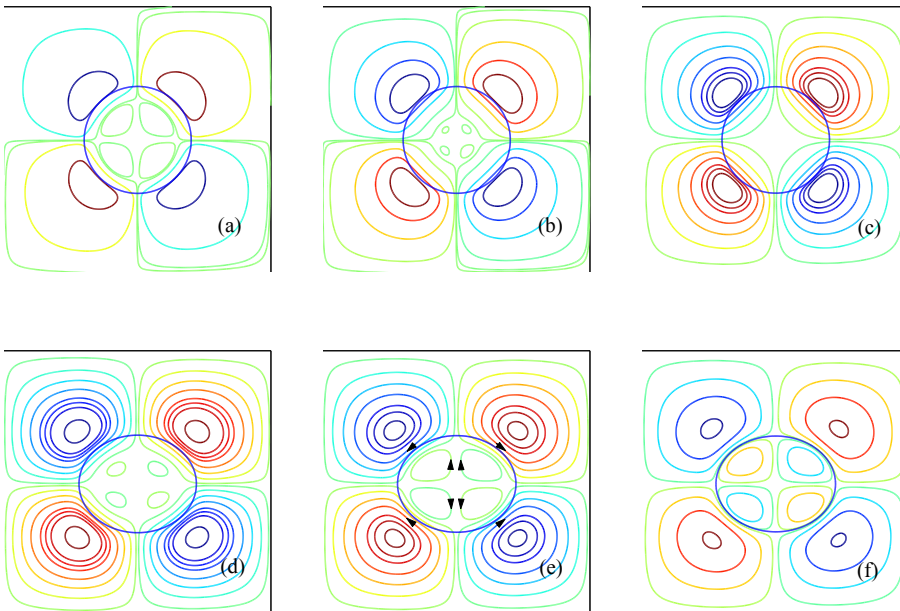
Figure 3: Evolution of the streamlines for a fluid system chosen from region (I) of the circulation-deformation map. Here, $R = 2$ and $S = 8$. The times are $t/\tau = 0.05$, 0.125, 0.263, 2.31, 2.8, and 7.5, where $\tau = (\mu_i + \mu_o)a/\gamma$ is a characteristic time. The time proceeds from the left to the right and the top to the bottom.

$u_\theta = U_{max} \sin 2\theta$, where θ is measured in counterclockwise direction from the top of the jet and

$$U_{max} = \frac{(S-R)u_s}{2(1+\widetilde{\mu})(1+R)^2}. \tag{8}$$

Accordingly, the maximum surface velocity takes place at angles $\pm\pi/4$ and $\pm 3\pi/4$. Here, $U_{max} = 0.0083$ and $\mathscr{D}_\infty = -0.11$. Furthermore, it appears that the position of the maximum velocity has shifted toward angles larger than $|\pi/4|$ and $|3\pi/4|$. It should be noted that $U_{max} > 0$ implies a fluid flow that runs from the top and the bottom toward the sides and $\mathscr{D} > 0$ implies prolate deformation, respectively. Conversely, $U_{max} < 0$ and $\mathscr{D} < 0$ imply fluid flow from the sides toward the top and the bottom and oblate deformation, respectively.

We also examined the evolution of the flow field for a fluid system from region (III) by considering $R = 8$ and $S = 2$. For this case, $U_{max} = -0.001$, $\mathscr{D}_\infty = 0.028$, and the evolution was similar to that seen in Fig. (3), except for the fact that the direction of flow circulation was the opposite and the interface deformed to a prolate. Furthermore, since the shear-driven velocity, as represented by $|U_{max}|$, was much weaker than that for the first simulation, no internal circulation appeared inside the jet at the early time. The small interface velocity for this case, compared to the first case, is due to the relatively high electric conductivity ratio, as is evident from Eq. (8) where it is seen that $U_{max} \sim 1/R^2$. This is, in turn, due to the fact that the net electric shear stress $[\![\tau_{r\theta}^e]\!] \sim 1/R^2$, which is the driver behind the tangential velocity, becomes weak as the jet fluid becomes more conductive [Reddy and Esmaeeli (2009)].

Next we examine the evolution of the flow field for a fluid system from region (II) by considering $R = 0.06$ and $S = 0.15$ [Fig. (4)]. Here, $U_{max} = -9.25 \times 10^{-4}$, $\mathscr{D}_\infty = 0.074$, and the shear-driven velocity is much weaker than that for the first simulation. Therefore, no vortices appear in the jet at the start of the motion ($t/\tau = 0.263$; frame a). However, contrary to the previous two cases, here the vortices gradually move inward ($t/\tau = 2.8, 3.07$, and 3.5; frames $b-d$). At this point a new set of vortices are generated in the outer flow to match the inner vortices ($t/\tau = 3.5$; frame d). As time passes, the inner vortices will be gradually confined within the jet and the outer vortices grow further ($t/\tau = 3.7, 7.5$; frames e and f). At steady state, no streamline crosses the interface as the interface cease to deform ($t/\tau = 7.5$; frame f). In passing, we should mention that the weak tangential velocity scale U_{max} seen for this case is typical for this region. This is evident from the circulation-deformation map where it is seen that the points on this region are close to the zero-circulation line ($\Phi_t \equiv R - S = 0$).

To explore the effect of Re_f on the evolution of the flow, we considered the same
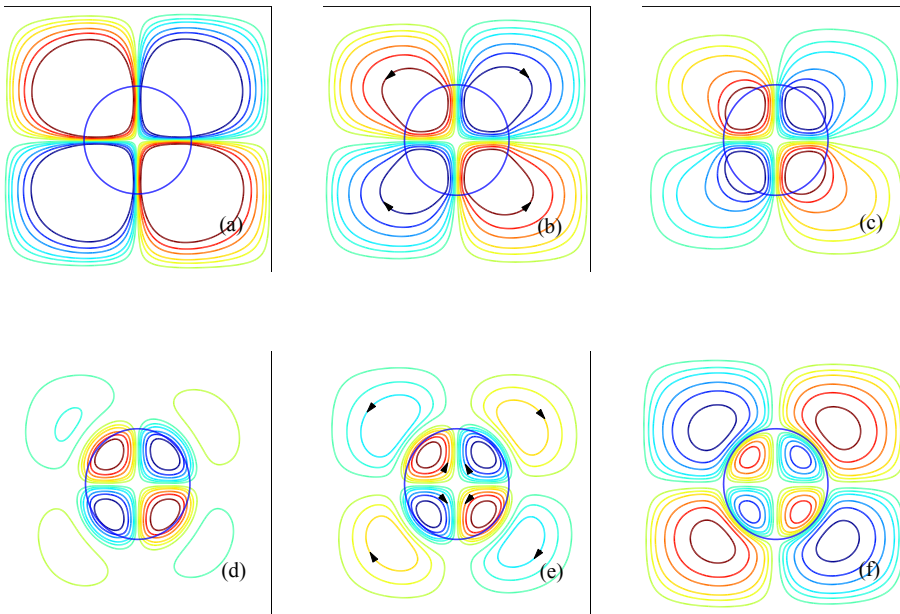
Figure 4: Evolution of the streamlines for a fluid system chosen from region (II) of the deformation map. Here, $R = 0.06$ and $S = 0.15$. The steady state deformation parameter is $\mathscr{D} = -9.25 \times 10^{-4}$. The times are $t/\tau = 0.263$, 2.8, 3.07, 3.5, 3.7, and 7.5 and proceed from the left to the right and the top to the bottom.

fluid systems as before, corresponding to regions (I), (II), and (III), and performed a set of simulations with $Re_f = 10$. Frame by frame analysis of the flow field for these cases showed that the evolution of the flow was essentially the same as the corresponding simulations for $Re_f = 1$, with the exception that the penetration of the crossing streamlines into the jet and their retreat was repeated a few times because of the nonmonotonic deformation of the interface. Figure (5) presents the effect of Re_f on the deformation-time history of the interface for the representative fluid systems from region (I) and (II). As is evident, an order of magnitude increase in the Reynolds number leads to nonmonotonic evolution of the deformation-time history. However, it does not affect the steady state deformation $\mathscr{D}_\infty$. Similarly, Fig. (6) presents the effect of Re_f on the kinetic energy of the fluid for the same cases. The kinetic energy is calculated using $KE = (1/2) \int_A \rho (u^2 + v^2) dA$, where u and v are the components of the velocity field in the horizontal and the vertical direction, and A is the area of the computational domain. The kinetic energy is scaled with $\rho_o u_s^2 A$, where $u_s = \varepsilon_a E_0^2 a / \mu_o$ is the velocity scale. The time is nondimensionalized
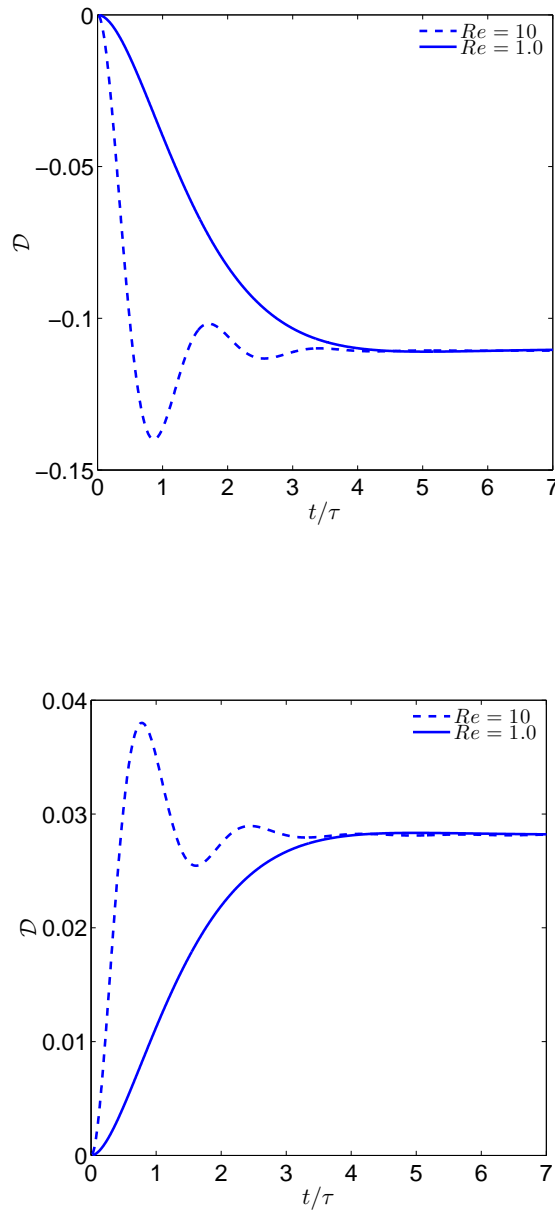
Figure 5: Effect of Re_f on the deformation-time history of the interface. The top and the bottom frames correspond, respectively, to fluid systems from region (I) and (II), respectively. The time is scaled by the characteristic time $\tau = (\mu_i + \mu_o)a/\gamma$ of the $Re_f = 1$ cases.
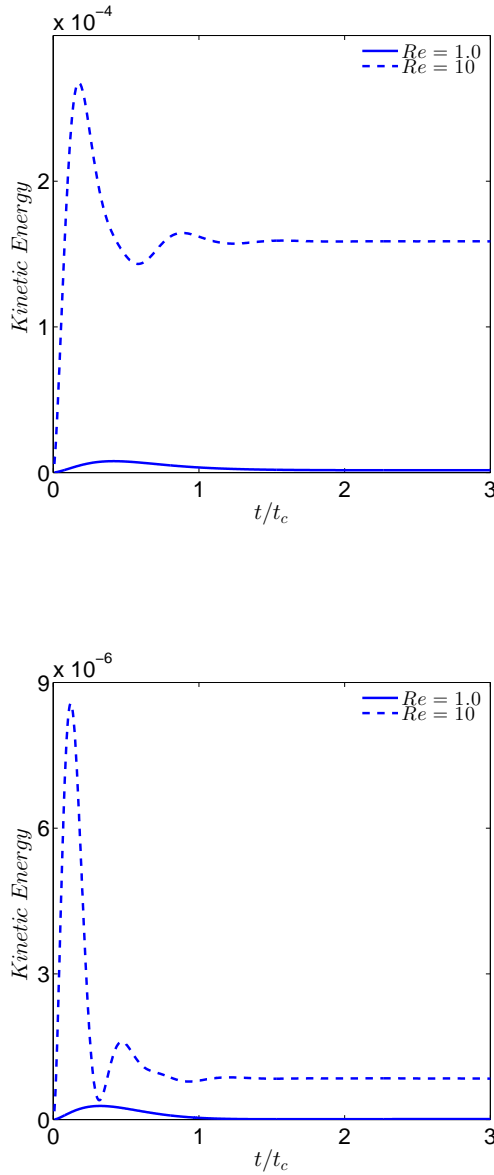
Figure 6: Effect of Re_f on the evolution of the kinetic energy of the fluids. The top and the bottom frames correspond, respectively, to the fluid systems from regions (I) and (II). The time is scaled by the convective time scale $t_c = a/u_s$.

with $t_c = a/u_s$ which is the convective time scale. For both $Re_f = 1$ and 10, the evolution of the kinetic energy is nonmonotonic. However, while for the $Re_f = 1$ case kinetic energy goes through a peak and settles to its steady state value, for the $Re_f = 10$ the kinetic energy is oscillatory. The nonmonotonic behavior of the kinetic energy is due to the fact that for finite Reynolds number ($Re_f \geq O(1)$) the time scale of momentum diffusion $t_d = a^2/\nu$ cannot be ignored compared to the convective time scale $t_c = a/u_s$; i.e., $Re_f = \rho a u_s/\mu = t_d/t_c$.

4.2   *Justification of the Observations Using Creeping Flow Solution*

Having explored the evolution of the flow field using the solution of the full Navier-Stokes equation, we now turn our attention to the evolution of the flow field for the same fluid systems using the creeping flow analytical solution of Esmaeeli and Sharifi (2011). The goal is to take advantage of the insight provided by the analytical formulation to further understand the underlying physics behind the previous observations. It should be emphasized that the analytical solution is based on the assumption of $Re \ll 1$ and $Oh^2 \gg 1$.

Figure (7) shows the evolution of the flow field for a fluid system corresponding to region (I) at the selected times noted in the caption. Here the domain is unbounded and, therefore, the flow field consists of open-ended streamlines that extend to infinity. Since for $Oh^2 \gg 1$ the time scale of diffusion of the momentum is negligibly small compared to the time scale of interface deformation, here the flow starts impulsively ($t = 0$ frame *a*). As time passes, the extended vortices gradually retreat from the jet, leaving behind four inner vortices (frame *b*). Here the dashed-line marks the dividing streamline (separatrix) that separates the inner vortices from the original extended vortices. Further outward displacement of the extended vortices leads to the continuous growth of the inner vortices until they occupy the jet (frame *c*). At steady state, the separatrix resides at the interface and the steady state flow pattern is similar to the corresponding schematic streamlines in Fig. (1). Furthermore, the interface deforms to an oblate.

We also examined the evolution of the flow field for the fluid systems corresponding to regions (II) and (III). For the latter, the evolution was essentially the same as that seen in Fig. (7). However, for the former, we could clearly see a trend similar to that observed in Fig. (4). Figure (8) shows a few frames about this case. Here as in Fig. (7) the flow is established impulsively and the initially extended vortices cross the interface. However, as time passes, the original extended vortices move gradually inward while the curvature of the streamlines that comprise the vortices continually increases (frame *b*). This transforms the open-ended vortices to closed vortices that are separated from a newly formed open-ended counterpart vortices by a dividing streamline. Here the scale of the figure obscures this development to be seen in

frame (*b*). However, further inward motion of the initially extended vortices makes the dividing streamline and the counterpart (extended) vortices visible (frame *c*). As time progress, the closed vortices are eventually confined inside the jet and the dividing streamline resides at the interface (frame *c*). At steady state, the sense of fluid flow is the same as the pertinent one depicted in Fig. (1). Furthermore, the interface deforms to a prolate.

To explore the reason for the observed differences, we examine the possibility of formation of the separatrix inside the jet ($j = i$) and in the ambient ($j = o$) by setting $f_j(r) = 0$ in the expressions for the streamfunction $\psi_j = f_j(r)\sin 2\theta$ ($j = i,o$); i.e., Eq. (9) and (10) of Esmaeeli and Sharifi (2011).

We first consider the streamfunction inside the jet. Setting $f_i(r) = 0$ leads to two roots, however, only one of them can possibly represent the radius of the circle $0 \leq r_{s_i} \leq 1$ that constitutes the separatrix

$$r_{s_i} = a\left[\frac{A_i + B_i\exp(-t/\tau)}{A_i + C_i\exp(-t/\tau)}\right]^{1/2} \equiv a\Lambda_i,$$

where (9)

$$A_i = -\frac{\Phi_t}{\Phi}, \quad B_i = 1, \quad C_i = \frac{1}{3}, \quad \Phi_t \equiv R - S.$$

In region (II), $\Phi_t/\Phi < 0$ according to Fig. (1) and, therefore, $A_i > 0$. Since $B_i > C_i > 0$ always, then $\Lambda_i > 1$ at all times. This implies that it is impossible to have a separatrix inside the jet. For regions (I) and (III), $\Phi_t/\Phi > 0$ according to Fig. (1)

(a)   (b)   (c)
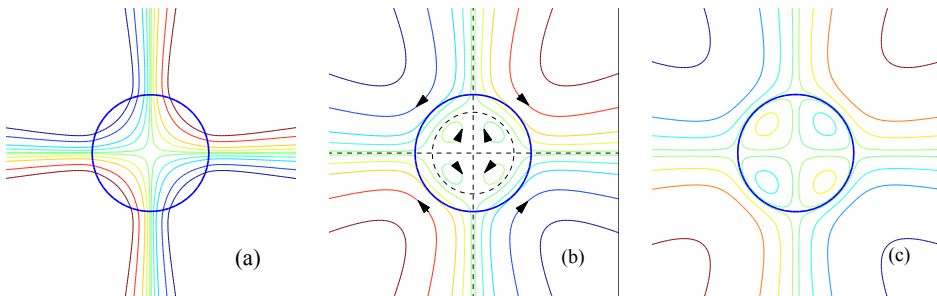
Figure 7: Evolution of the streamlines for a fluid system chosen from region (I) of the circulation-deformation map. Here, $R = 2$, $S = 8$, $\tilde{\rho} = 1$, $\tilde{\mu} = 1.0$, and $Oh = 4.5$. The times are $t = 0$, 1.6τ, and 8τ, where $\tau = (\mu_i + \mu_o)a/\gamma$ is the characteristic time of the problem. Here the steady state deformation parameter is $\mathscr{D} = -0.005$. Other nondimensional numbers are $Re_f = 4 \times 10^{-4}$, $Ca = 0.008$, and $Re_{el} = 2 \times 10^{-4}$.

and, therefore $A_i < 0$. Thus, we need to evaluate the various possibilities concerning the signs and magnitudes of the $N_i \equiv A_i + B_i \exp(-t/\tau)$ and $D_i \equiv A_i + C_i \exp(-t/\tau)$. Since $B_i > C_i > 0$, then N_i is always greater than D_i. However, we cannot draw a definite conclusion regarding the signs of N_i and D_i. Three possibilities exist: (1) if $[N_i < 0, D_i < 0]$, then $\Lambda_i \equiv \sqrt{N_i/D_i} < 1$ for all times. Therefore, there exists a dividing streamline inside the jet at $t = 0$; (2) if $[N_i > 0, D_i < 0]$ or (3) $[N_i > 0, D_i > 0]$, then the dividing streamline does not exist initially but it can form at some
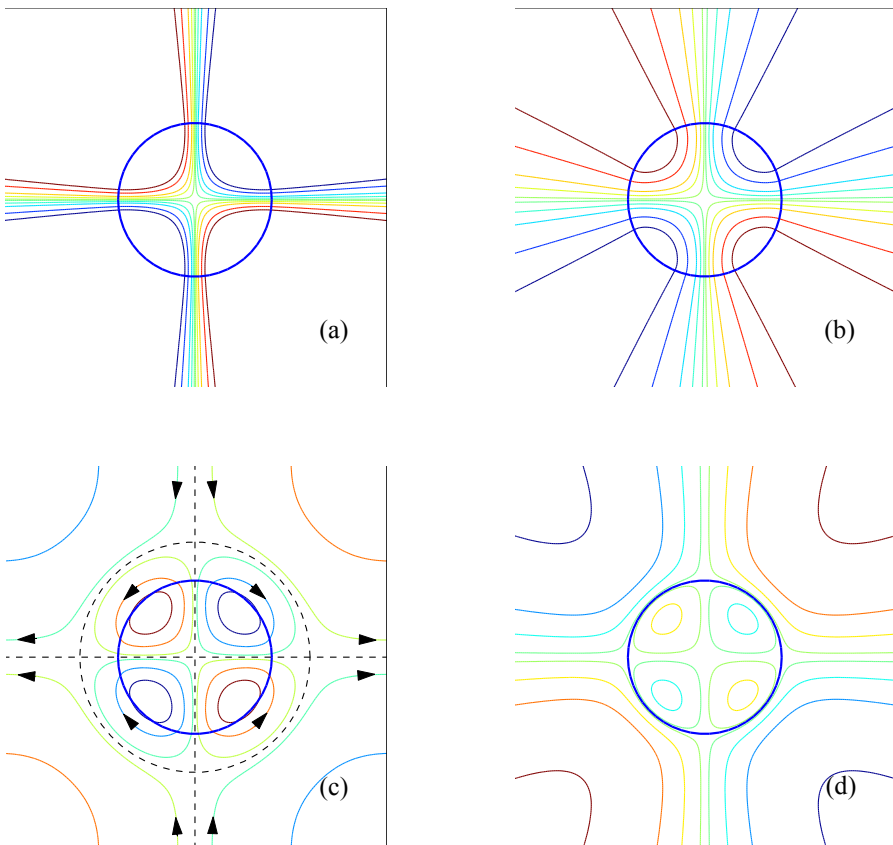
Figure 8: Evolution of the streamlines for a fluid system chosen from region (II) of the deformation map. Here, $R = 0.06$, $S = 0.15$, $\widetilde{\rho} = 1$, $\widetilde{\mu} = 1$, and $Oh = 4.5$. The steady state deformation parameter is $\mathscr{D} = 0.0015$. The times are $t = 0$, τ, 2.35τ, and 8τ. The time proceeds from left to right and top to bottom. Other nondimensional numbers are $Re_f = 4 \times 10^{-4}$, $Ca = 0.008$, and $Re_{el} = 2 \times 10^{-4}$

later time with infinitesimally small radius ($r_{s_i} \to 0$):

$$t_{0_i} = \tau \ln\left(\frac{\Phi}{\Phi_t}\right). \tag{10}$$

Here, $dr_{s_i}/dt > 0$ and, therefore, the radius of the dividing streamline increases monotonically until it resides at the interface, supporting the observation (seen in Fig. (7)) that the inner vortices will be formed inside the jet and then grow outward to occupy the jet.

Turning our attention to the streamfunction for the ambient flow and setting $f_o(r) = 0$ yields the radius of the circle $r_{s_o} \geq 1$ that can possibly represent the separatrix:

$$r_{s_o} = a\left[\frac{A_o + B_o \exp(-t/\tau)}{A_o + C_o \exp(-t/\tau)}\right]^{1/2} \equiv a\Lambda_o,$$

where

$$A_o = \frac{\Phi_t}{\Phi}, \quad B_o = \frac{1}{3}, \quad C_o = 1. \tag{11}$$

Here the analysis is straightforward for regions (I) and (III), where always $A_o > 0$ and $C_o > B_o > 0$. Then, $\Lambda_o < 1$ at all times, which implies that it is impossible to have a dividing streamline in the ambient flow for these two regions. For region (II), we need to evaluate the various possibilities concerning the signs and magnitudes of $N_o \equiv A_o + B_o \exp(-t/\tau)$ and $D_o \equiv A_o + C_o \exp(-t/\tau)$, since $A_o < 0$. Two
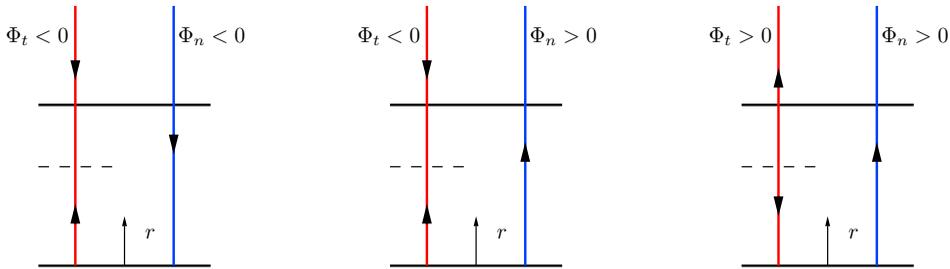
Figure 9: A schematic figure depicting the superposition of the shear-driven (Φ_t) and deformation-driven (Φ_n) flows along the north pole. The first and the third frames correspond, respectively, to the flows in regions (I_b) and (III), and the second frame corresponds to the flow in regions (I_s) and (II). The lower and the upper horizontal lines represent, respectively, the y coordinates of the center and the surface of the jet (at the top) and the dashed line shows the approximate position of the dividing streamline in the shear-driven flow.

possibilities exist: (1) if $[N_o < 0$ and $D_o < 0]$, then $\Lambda_o = \sqrt{N_o/D_o} > 1$ and there exists a dividing streamline outside the jet at $t = 0$ with finite radius; (2) if $[N_o > 0$ and $D_o < 0]$ or $[N_o > 0$ and $D_o > 0]$, then the dividing streamline does not exist at the beginning of the evolution but it will form at some later time far away (i.e., $r_{s_o} \to \infty$) from the interface:

$$t_{0_o} = \tau \ln \left(-\frac{\Phi}{\Phi_t} \right) \tag{12}$$

Here $dr_{s_o}/dt < 0$ and, therefore, the radius of the dividing streamline decreases monotonically until it resides at the interface, supporting the observation (seen in Fig. (8)) that the originally extended vortices gradually transform to closed vortices and move into the jet.

From the analysis so far, it is clear that the evolution of the flow field is closely related to the formation of the dividing streamline. As such, understanding the underlying mechanism behind the formation of the dividing streamline will be helpful in predicting the flow evolution. Here we lay out a methodology that is based on physical reasoning and can be used to analyze the current problem as well as the more complex circumstances where mathematical reasoning will be tedious. To this end, we note that the drivers behind the fluid flow (as well as the interface deformation) during the transient are the net normal and tangential electric stresses, $[[\tau_{rr}^e]]$ and $[[\tau_{r\theta}^e]]$, as given by Eq. (7) and (8) of Esmaeeli and Sharifi (2011), where the double bracket denotes the jump in a physical parameter at interface. Since the sense of fluid flow driven by the individual stresses ($[[\tau_{r\theta}^e]]$ and $[[\tau_{rr}^h]]$) can be figured out qualitatively, the superposition of the two flow fields can help to understand the overall flow pattern; i.e. $\mathbf{u} \sim \mathbf{u}_t + \mathbf{u}_n$. Here we denote the flow due to $[[\tau_{r\theta}^e]]$ and $[[\tau_{rr}^h]]$ as the shear- and the deformation-driven flows, respectively. During the transient, the senses of the shear- and deformation-driven flows are determined by the signs of $\Phi_t = R - S$ and $\Phi_n = \Phi - \Phi_t$, respectively, and their strengths are proportional to $|\Phi_t|$ and $|\Phi_n|$. Furthermore, the shear-driven flow pattern for all the fluid systems is similar to the flow pattern seen for region (I) in frame (b) of Fig. (7), with the exception that the senses of the flow for fluid systems chosen from region (III) will be the opposite to that depicted in this panel. Similarly, the deformation-driven flow pattern will be similar to the first frame of Fig. (7) or (8), except that the streamlines will be more bent; thus, for fluid systems chosen from regions (II) and (III), where the interface is deformed to a prolate, the initially extended vortices cross into the interface at the sides and exit at the top and the bottom. Conversely, for a fluid system chosen from region (I), where the interface deforms to an oblate, the direction of the flow is the opposite.

To examine the results of the superposition of the shear- and deformation-driven

flow patterns, rather than considering the whole flow field, we focus on the super-position of a representative streamline from each flow in the upward direction along the vertical line that passes through the center of the jet. This makes the analysis much simpler and is valid since the dividing streamline is circular. We further note that along the dividing streamline the radial component of the velocity u_r is zero. Thus, the dividing streamline will form whenever the radial velocity vanishes be-cause of the superposition of the two flow fields; i.e., $u_{r_t} + u_{r_n} = 0$. To proceed further, we need to include the $\Phi_n = 0$ curve in the circulation-deformation map so that the map will be well-suited for transient flows. As shown in Fig. (1), this leads to the division of region (I) to a big (I_b) and a small (I_s) region, but does not affect the structure of regions (II) and (III). The new regions can be defined:

$$\text{Region } I_s: \qquad \frac{1}{3}(R^2 + R + 1) < S < \frac{1}{2}(R^2 + 1);$$

$$\text{Region } I_b: \qquad S > \frac{1}{2}(R^2 + 1). \tag{13}$$

Geometrically, region I_b is confined between $\Phi_n = 0$ curve and lines $\overline{cd}$ and $\overline{de}$ and region I_s is confined between $\Phi = 0$ and $\Phi_n = 0$ curves and the lines $\overline{bc}$ and $\overline{ef}$. Here four possible senses of flow patterns and interface deformation exists according to the signs of Φ_t and Φ_n.

Figure (9) shows schematically the radial components of the shear-driven and the deformation-driven velocities; u_{r_t} and u_{r_n}, respectively. The analysis is relatively simple for regions (III) and (I_b). For these regions, the senses of shear-driven and deformation-driven flows are the same in the ambient fluid and, therefore, there is not a possibility for the formation of a dividing streamline there. However, the direction of the Φ_n-driven velocity is the opposite to that of the Φ_t-driven velocity in part of the jet. Thus, it is possible for a dividing streamline to form in the jet because of competition of the opposing streamlines. These conclusions are in line with the results of Eq. (9) and (11). On the other hand, for regions (II) and (I_s) the directions of the Φ_n-driven and Φ_t-driven velocities are the opposite both in the ambient and part of the jet. This suggests that there is a possibility of formation of a dividing streamline "both" in the ambient and the jet. This observation seems in contradiction with the results of Eq. (9) and (11), where we showed that for regions (II) and (I) the dividing streamline is possible "either" in the ambient or inside the jet, respectively. This apparent discrepancy can be resolved easily considering the following facts. First, inside the jet, the dividing streamline will exist if the Φ_n-driven radial velocity is sufficiently weak so that it will only nullify "part" of the opposing Φ_t-driven radial velocity or it does not nullify it at all. On the other hand, if Φ_n-driven radial velocity is sufficiently strong so that it nullifies the "whole" op-posing Φ_t-driven radial velocity, the dividing streamline will be pushed out from

the jet into the ambient. Inspection of Fig. (1) shows that this is indeed the case for region (II). For this region, $|\Phi_n|$ is dominant over $|\Phi_t|$ since here the fluid velocity, running from the top and the bottom to the sides, tends to deform the interface to an oblate but the interface actually deforms to a prolate. Considering the fact that $|u_{r_n}| \sim |\Phi_n|$ and $|u_{r_t}| \sim |\Phi_t|$, then $|u_{r_n}|$ can override $|u_{r_t}|$, pushing the dividing streamline into the ambient. On the other hand for region (I_s), $|\Phi_n|$ is weak since it tends to deform the interface to a prolate, but the interface actually deforms to an oblate. Thus, for this region, $|u_{r_n}|$ can at most nullify part of the opposing $|u_{r_t}|$, leading to possible displacement of the dividing streamline in the jet.

In summary, the results of flow superposition are in line with those of the mathematical derivation for all the regions. This is encouraging since for more complex flows where the mathematical derivation becomes tedious, the superposition technique will likely to be an effective means for gaining insight into the flow pattern.

5   Conclusion

The evolution of the flow field during the transient electrohydrodynamics of a liquid jet can find relevance in microfluidic applications that are aimed to enhance heat and mass transfer or chaotic mixing using electric field. The phenomenon has not been explored in detail before and was subject of this study. The computational results showed that the flow evolution is determined by the relative importance of the ratio of electric conductivity R and permittivity S. For fluid systems that belong to region (I) and (III) of the circulation-deformation map, the flow evolves as a result of growth of vortices that are formed inside the jet. On the other hand, for fluid systems that belong to region (II), the flow evolves as a result of the growth of vortices that are formed in the ambient and penetrate into the jet until they are confined within the jet.

Examination of the results of the analytical solution of the problem [Esmaeeli and Sharifi (2011)] for flows with $Re \ll 1$ and $Oh^2 \gg 1$ showed that the flow evolution was similar to the corresponding computational one for finite Reynolds and $O(1)$ Ohnesorge number. Inspection of the analytical results and the pertinent equations showed that the flow field evolves as a result of the interplay of the deformation-driven and (electric) shear-driven flows and that through the superposition of these flows one can qualitatively predict the evolution of the flow field.

References

Esmaeeli, A.; Sharifi, P. (2011):   The transient dynamics of a liquid column in a uniform transverse electric field of small strength.   *J. Electrostat.*, vol. 69, no. 6, pp. 504 – 511.

Halim, M. A.; Esmaeeli, A. (2013): Computational studies on the transient electrohydrodynamics of a liquid drop. *FDMP: Fluid Dynamics & Materials Processing*, vol. 9, no. 4, pp. 435–460.

Reddy, M.; Esmaeeli, A. (2009): The ehd-driven fluid flow and deformation of a liquid jet by a transverse electric field. *Int. J. Multiphase Flow*, vol. 35, pp. 1051–1065.

Subramanian, R.; Jog, M. A. (2005): Heat and mass transfer to a translating drop in an electric field. *J. Heat Trans-T ASME*, vol. 127, pp. 1087–1095.

Taylor, G. (1966): Studies in electrohydrodynamics: I. the circulation produced in a drop by an electric field. *Proc. Roy. Soc. A.*, vol. 291, pp. 159–167.

Ward, T.; Homsy, G. M. (2006): Chaotic streamlines in a translating drop with a uniform electric field. *J. Fluid Mech.*, vol. 547, pp. 215–230.